



# Nanostructured Fe<sub>3</sub>O<sub>4</sub>@C as anode material for lithium-ion batteries



Zhipeng Zeng<sup>a</sup>, Hailei Zhao<sup>a, b, \*</sup>, Jie Wang<sup>a</sup>, Pengpeng Lv<sup>a</sup>, Tianhou Zhang<sup>a, b</sup>, Qing Xia<sup>a</sup>

<sup>a</sup> School of Materials Science and Engineering, University of Science and Technology Beijing, Beijing 100083, China

<sup>b</sup> Beijing Key Lab of New Energy Materials and Technologies, Beijing 100083, China

## HIGHLIGHTS

- Fe<sub>3</sub>O<sub>4</sub>@C was prepared via a facile, economical and one-pot solvothermal route.
- Fe<sub>3</sub>O<sub>4</sub>@C spheres present nano-porous and mosaic structured morphology.
- High specific capacity ( $\sim 1000 \text{ mAh g}^{-1}$ ) and excellent rate-capability were achieved.
- Porous carbon matrix ensures a stable cycling performance.

## ARTICLE INFO

### Article history:

Received 17 June 2013

Received in revised form

27 August 2013

Accepted 15 September 2013

Available online 22 September 2013

### Keywords:

Magnetite

Active carbon

Electrochemical properties

Anode materials

Lithium ion batteries

## ABSTRACT

The active particle cracking and electrode pulverization of iron oxide anode material as a result of volume expansion during charge/discharge process cause poor reversibility and significant capacity fading in rechargeable lithium-ion batteries. Here, we demonstrate a facile solvothermal route to immobilize the Fe<sub>3</sub>O<sub>4</sub> particles on the porous active carbon. The present method enables us to obtain nano-porous and mosaic structured Fe<sub>3</sub>O<sub>4</sub>@C spheres with an average size of *ca.* 100 nm. The porous active carbon plays an important role in the improvement of electrochemical properties of Fe<sub>3</sub>O<sub>4</sub>. It not only acts as a host for the deposition of Fe<sub>3</sub>O<sub>4</sub> particles, but also provides void spaces for active Fe<sub>3</sub>O<sub>4</sub> to buffer the volume expansion. The good contact between Fe<sub>3</sub>O<sub>4</sub> and active carbon ensures the fast electron/Li-ion transport. As a result, the porous Fe<sub>3</sub>O<sub>4</sub>@C shows a high reversible specific capacity of  $\sim 1000 \text{ mAh g}^{-1}$ , good cycle stability and excellent rate capability. Therefore, we believe that this composite is a potential candidate for anode material of high-energy lithium-ion battery.

© 2013 Elsevier B.V. All rights reserved.

## 1. Introduction

Lithium ion batteries (LIBs) continue to draw attention because advanced energy storage devices with higher energy and power density and longer lifetime are required for many applications, such as portable electronics, electric tools, electric vehicles (EVs) and hybrid electric vehicles (HEVs) [1–4]. They are also being seriously considered for the efficient storage and utilization of intermittent renewable energies like solar and wind [5–7]. The conventional anode materials based on graphite cannot satisfy the ever-growing demands of high energy density batteries due to the limited specific capacity ( $\sim 372 \text{ mAh g}^{-1}$ ). It is essential, therefore, to explore new anode materials with exceptional capacity multiple times of graphite as well as excellent rate capability and long cycling lifetime [8–10]. Transition metal oxides (MO, M = Cu, Co, Fe, Mo, Ni)

[10] are attractive anode materials because they have lithium storage ability at their nano scales and show high reversible capacity ( $500\text{--}1000 \text{ mAh g}^{-1}$ ) and acceptable lithiation potentials [1,9–12]. Among these potential anode materials, Fe<sub>3</sub>O<sub>4</sub> is even promising in virtue of its unique features, such as high theoretical capacity ( $926 \text{ mAh g}^{-1}$ ), good electronic conductivity, lower cost, environmental friendliness and natural abundance [12–14]. However, similar to other oxides, Fe<sub>3</sub>O<sub>4</sub> also suffers from large volume change during lithiation/delithiation process, which can lead to active particle cracking, electrode pulverization, and subsequent loss of electrical contact between active material and current collector, eventually result in poor reversibility and rapid capacity degradation. The continuous active particle cracking causes also an unstable solid electrolyte interphase (SEI) film. Accordingly, it is crucial to take approaches to relieve the volume change, maintain the integrity of the electrodes and thereby improve the cycling stability of electrode [15].

Many strategies have been proposed to overcome this issue, such as nanostructuring, carbon coating, and nanocompositing [14,16,17]. The hollow and porous structures are attractive particle

\* Corresponding author. School of Materials Science and Engineering, University of Science and Technology Beijing, Beijing 100083, China. Tel./fax: +86 10 82376837.

E-mail addresses: [hlzhao@ustb.edu.cn](mailto:hlzhao@ustb.edu.cn), [hlzhao66@gmail.com](mailto:hlzhao66@gmail.com) (H. Zhao).

morphology, which can provide void spaces to buffer the large volume expansion [18,19] encountered by the large capacity active materials, such as transition metal oxides, Si- and Sn-based materials. Recently, Lim et al. prepared hollow  $\text{Fe}_3\text{O}_4$  microspheres by ionic adsorption technique, which exhibited high reversible capacity and enhanced cycling stability [8]. Chen and co-workers synthesized porous hollow  $\text{Fe}_3\text{O}_4$  beads, which showed good cycling stability but relatively lower specific capacity,  $500 \text{ mAh g}^{-1}$  after 50 cycles at  $100 \text{ mA g}^{-1}$  [20]. Compositing with carbon has also been proven to be an effective modification technique to enhance the electrochemical performance of iron oxides anode materials [13,21,22]. For example, coating carbon layer on particle surface cannot only facilitate ion and electron transport, but also prevent electrochemical aggregation and accommodate part of the volume change of active materials during lithium ion insertion/extraction. Several types of carbon coated  $\text{Fe}_3\text{O}_4$  with particle shape of nanospindles [12], nanorods [23,24] and microcapsules [25] have shown improved cycle performance. On the other hand, various porous carbons, such as mesocellular carbon [26], carbon fiber network [27] and carbon foam [28], were prepared as host to accommodate  $\text{Fe}_3\text{O}_4$  nanoparticles, forming  $\text{Fe}_3\text{O}_4/\text{C}$  composite.

More recently, graphene has aroused much interest as carbon matrix or additive of electrode material for its ultrahigh specific area and excellent electronic conductivity. Graphene-wrapped  $\text{Fe}_3\text{O}_4$  [14], graphene nanosheets- $\text{Fe}_3\text{O}_4$  [29], and graphene- $\text{Fe}_3\text{O}_4$  nanocomposites [30] have been fabricated with various sizes and shapes. A latest research by Wang's group reported a composite of  $\text{Fe}_3\text{O}_4$  nanoparticles grown on graphene, which displayed an excellent electrochemical performance as supercapacitor electrode [31]. The honeycomb-structured graphene provides large surface to well anchor  $\text{Fe}_3\text{O}_4$  particles, and affords an elastic buffer to alleviate the volume variations. In addition, the graphene as an excellent conductive agent can support a highway for electron transport and thereby provide an excellent rate capability for electrode.

Taking an overview of the current research, hydrothermal method is a most common way to synthesize composite with carbon matrix by adding carbon source like glucose, sucrose or graphene into the reaction solution. However, a post heat-treatment is usually required to realize the organics decomposition and carbonization, which makes the synthesis process much tedious. In this study, we developed a one-pot solvothermal route to synthesize  $\text{Fe}_3\text{O}_4/\text{C}$  nanocomposite by introducing cheaper active carbon as a carrier, on the surface of which  $\text{Fe}_3\text{O}_4$  particles were deposited. The active carbons have huge specific surface area because of their controlled distribution of pores [32,33]. Therefore, a good electrochemical performance can be expected by dispersing  $\text{Fe}_3\text{O}_4$  particles into the pores of active carbon. The large specific surface area and the micropores of active carbon can help to fix the  $\text{Fe}_3\text{O}_4$  particles under solvothermal condition and to accommodate the volume change of  $\text{Fe}_3\text{O}_4$  occurring in the lithium ion insertion/extraction process. As shown in the results, the prepared  $\text{Fe}_3\text{O}_4/\text{C}$  composite exhibits a high specific capacity, good cycling stability and excellent rate capability.

## 2. Experimental section

### 2.1. Synthesis of $\text{Fe}_3\text{O}_4/\text{C}$ and bare $\text{Fe}_3\text{O}_4$

$\text{Fe}_3\text{O}_4/\text{C}$  composite material was synthesized via a solvothermal method with  $\text{FeCl}_3$  as iron resource. The amount of  $2.7 \text{ g}$   $\text{FeCl}_3$  was dissolved in  $30 \text{ ml}$  of ethylene glycol under magnetic stirring to form a homogeneous yellow solution A. Solution B was prepared by dissolving  $12 \text{ g}$  of  $\text{NaAc} \cdot 3\text{H}_2\text{O}$  (as precipitant) and  $2 \text{ g}$  of polyethylene glycol (PEG200, as dispersant) in  $40 \text{ ml}$  of ethylene glycol. The two solutions were mixed together by adding solution B

dropwise into solution A to produce brown solution. After a vigorous stirring,  $0.3 \text{ g}$  of active carbon was dispersed into the mixture solution under ultrasonic stirring. The resultant suspension was transferred to a  $100 \text{ ml}$  Teflon-lined stainless steel autoclave, which was sealed and heated at  $200^\circ\text{C}$  for  $48 \text{ h}$  in electronic oven. After solvothermal treatment, the autoclave was allowed to cool to room temperature naturally. Some black products were produced, which were collected by centrifugation, washed with distilled water and ethanol for several times, and then dried in a vacuum environment at  $70^\circ\text{C}$  for  $6 \text{ h}$ . Finally, the  $\text{Fe}_3\text{O}_4/\text{C}$  powder was obtained. As comparison, bare  $\text{Fe}_3\text{O}_4$  was also prepared by the identical procedures for  $\text{Fe}_3\text{O}_4/\text{C}$  composite except for the addition of active carbon.

### 2.2. Structure characterization

The phase structure of the samples was identified by X-ray diffraction (XRD, Rigaku, D/max-A,  $\text{Cu K}\alpha$ ,  $\lambda = 1.5406 \text{ \AA}$ ) and Raman spectroscopy (Renishaw RM 2000, excited by  $632.8 \text{ nm}$  He–Ne laser). The particle morphology and the lattice structure of the synthesized samples were characterized by field-emission scanning electron microscope (FE-SEM, SUPRA55) and high resolution transmission electron microscope (HRTEM, JEM-2010,  $200 \text{ kV}$ ). Energy-dispersive X-ray spectroscopy-scanning transmission electron microscope (EDX-STEM) mapping was performed on a Tecnai F20 filed emission transmission electron microscope operated at  $200 \text{ keV}$ . The surface area and pore size distribution of active carbon were determined by  $\text{N}_2$  adsorption-desorption technique (QUADRASORB SI-MP, Quantachrome). The Brunauer–Emmett–Teller (BET) surface area and pore size distribution plot were calculated by applying the linear part of the BET plot and the Barrett–Joyner–Halenda (BJH) model, respectively. Thermogravimetric (TG) analysis of the  $\text{Fe}_3\text{O}_4/\text{C}$  was investigated on an STA 449F3 TG-differential scanning calorimetry (DSC) apparatus (Netzsch) with a heating rate of  $10^\circ\text{C}$  per minute from room temperature to  $600^\circ\text{C}$  in air atmosphere.

### 2.3. Electrochemical measurements

The electrochemical properties of the prepared  $\text{Fe}_3\text{O}_4/\text{C}$  and bare  $\text{Fe}_3\text{O}_4$  samples as anode materials of lithium ion cells were evaluated by galvanostatic charge/discharge technique. The working electrodes were prepared by mixing  $80 \text{ wt } \%$  active material (bare  $\text{Fe}_3\text{O}_4$  particles or  $\text{Fe}_3\text{O}_4/\text{C}$  composite powder after solvothermal treatment) with  $10 \text{ wt } \%$  acetylene black (AB) as conductive agent and  $10 \text{ wt } \%$  carboxymethylcellulose (CMC) dissolved in distilled water as binder. The formed homogeneous slurry was pasted on copper foil and dried in an oven to remove the possible solvent. The electrode was then pressed and punched into circular discs with a diameter of  $8 \text{ mm}$  for cells assemble before dried further under vacuum at  $120^\circ\text{C}$  for  $24 \text{ h}$ . The weight of active materials in each disc was  $1.2\text{--}2 \text{ mg cm}^{-2}$ . The cells were finally assembled in an Ar-filled glove box with the  $\text{Fe}_3\text{O}_4/\text{C}$  composite or bare  $\text{Fe}_3\text{O}_4$  particles as test electrode, pure lithium foil as counter electrode and porous polypropylene film (Celgard 2400) as separator. The nonaqueous electrolyte used was  $1 \text{ M LiPF}_6$  dissolved in ethylene carbonate (EC), diethyl carbonate (DEC) and dimethyl carbonate (DMC) ( $1:1:1$ , in vol %). Cycling tests were performed galvanostatically on a battery test system (LAND CT-2001A tester) in the voltage range of  $0.02\text{--}3.0 \text{ V}$  (vs.  $\text{Li/Li}^+$ ) at room temperature. To evaluate the rate performance, the cell was cycled at different current densities, varying from  $100$  to  $1000 \text{ mA g}^{-1}$ . The electrochemical impedance spectra (EIS) measurements were carried out in Solartron 1260 Frequency Response Analyzer combined with a Solartron 1287 potentiostat in the frequency region from  $10^5$  to

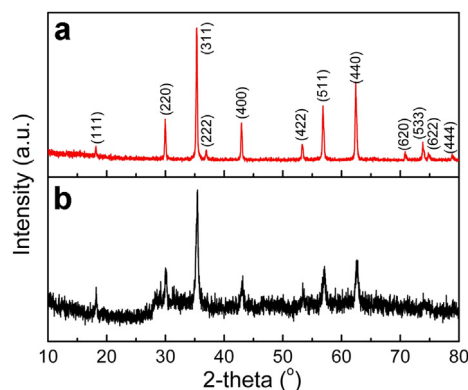


Fig. 1. XRD patterns of bare Fe<sub>3</sub>O<sub>4</sub> particles (a) and Fe<sub>3</sub>O<sub>4</sub>@C composite (b).

0.01 Hz with a signal amplitude of 5 mV. To investigate the structural integrity of electrode film, the Swagelok-type cells with Fe<sub>3</sub>O<sub>4</sub> and Fe<sub>3</sub>O<sub>4</sub>@C as working electrode were also assembled. After charge/discharged at 100 mA g<sup>-1</sup> for 10 cycles, the cells were disassembled inside an argon-filled glove box and the electrodes were washed carefully with DMC in order to remove electrolyte residues. The dried electrode films were subjected to various structural characterizations.

### 3. Results and discussion

Fig. 1 shows the XRD patterns of the Fe<sub>3</sub>O<sub>4</sub> and Fe<sub>3</sub>O<sub>4</sub>@C powders prepared at 200 °C for 48 h. All the diffraction peaks in Fig. 1a could be well indexed to Fe<sub>3</sub>O<sub>4</sub> (JCPDS No. 76-1849), indicating the successful synthesis of Fe<sub>3</sub>O<sub>4</sub> powders. For the XRD spectrum of the Fe<sub>3</sub>O<sub>4</sub>@C (Fig. 1b), the main peaks are similar to that of the pristine Fe<sub>3</sub>O<sub>4</sub> powders but have a weak peak intensity and wide FWHM (full width at half maximum), which is mainly resulted from the smaller particle size of Fe<sub>3</sub>O<sub>4</sub> in Fe<sub>3</sub>O<sub>4</sub>@C composite (as revealed by FE-SEM observation, Fig. 4). High background can be obviously recognized for sample Fe<sub>3</sub>O<sub>4</sub>@C, which should originate from the presence of amorphous carbon [14]. The existence of carbon in Fe<sub>3</sub>O<sub>4</sub>@C composite is further confirmed by Raman spectroscopic analysis. As shown in Fig. 2, the characteristic D and G bands observed at 1348 and 1592 cm<sup>-1</sup> belong to the disordered and graphitic carbon, respectively, which are in good correspondence with the reported values [14,25,29,34].

The carbon content of the synthesized Fe<sub>3</sub>O<sub>4</sub>@C composite was disclosed by TG/DSC analysis. As illustrated in Fig. 3, the initial weight loss of ca. 3.66 wt % from 50 to 300 °C should correspond to

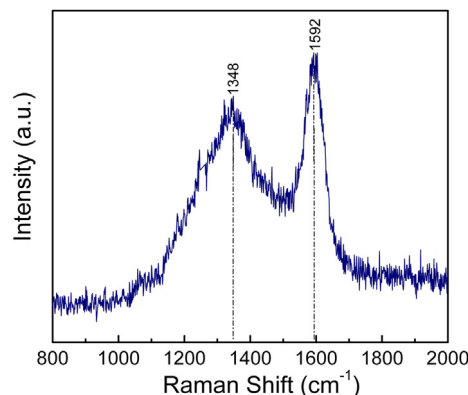


Fig. 2. Raman spectrum of Fe<sub>3</sub>O<sub>4</sub>@C composite.

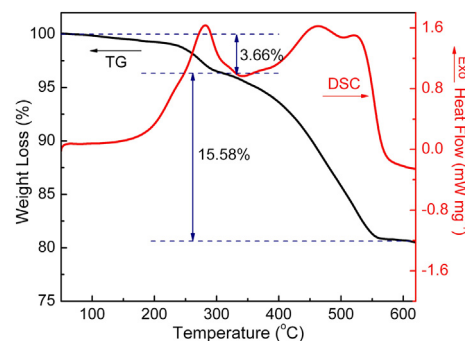


Fig. 3. TG-DSC curves of the Fe<sub>3</sub>O<sub>4</sub>@C composite.

the evaporation of the weakly adsorbed water and solvent as well as the oxidation of some remained organic groups [35–38]. With increasing temperature, an obvious weight loss occurs near 300 °C extending to 550 °C, accompanying with two exothermic peaks at 460 and 520 °C in the DSC curve. This weight loss should correspond to two physicochemical processes, the oxidations of carbon and Fe<sub>3</sub>O<sub>4</sub>. The oxidation of carbon to CO<sub>2</sub>/CO causes weight loss, while the oxidation of Fe<sub>3</sub>O<sub>4</sub> to Fe<sub>2</sub>O<sub>3</sub>, which occurs when the temperature is higher than 500 °C [39], results in weight gain. No obvious and independent weight gain could be observed since the two processes take place in a mixed mode and the weight loss plays a dominant role. From the whole weight loss of 15.58 wt %, the carbon content in the Fe<sub>3</sub>O<sub>4</sub>@C composite can be derived to be about 18 wt % and the mass ratio of the Fe<sub>3</sub>O<sub>4</sub> is about 78%.

The particle morphology of the active carbon with and without solvothermal treatment, and the synthesized bare Fe<sub>3</sub>O<sub>4</sub> and Fe<sub>3</sub>O<sub>4</sub>@C nanocomposite powders were observed with FE-SEM. Fig. 4a and b show the active carbon particles before and after solvothermally treated at 200 °C for 48 h. The active carbon displays a blob-like particle shape with irregular particles aggregating together. After solvothermal treatment, active carbon exhibits an obvious appearance change. The blob-like particles change to be much smaller (~100 nm) and become sphere-like particles with uniform particle size distribution, which may be related to the recrystallization of active carbon under solvothermal condition. With respect to the bare Fe<sub>3</sub>O<sub>4</sub>, it shows a well-defined spherical particle shape with size of ca. 500 nm, as depicted in Fig. 4c. After addition of active carbon into the solvothermal solution, the synthesized Fe<sub>3</sub>O<sub>4</sub>@C sample (Fig. 4d) presents a granular particles with size slightly larger than that of the solvothermally treated active carbon (Fig. 4b) but much smaller than the bare Fe<sub>3</sub>O<sub>4</sub> (Fig. 4c), implying that the active carbon can play as a nucleus to promote the crystallization of Fe<sub>3</sub>O<sub>4</sub> from solution and limit the growth and aggregation of the crystallized nano-Fe<sub>3</sub>O<sub>4</sub> grains.

To further characterize the microstructure of the synthesized Fe<sub>3</sub>O<sub>4</sub>@C sample, TEM and HR-TEM inspections were conducted. Fig. 5a shows the TEM image of the solvothermally treated active carbon, a lot of micropores could be observed. The porous feature of the active carbon was further investigated by Brunauer–Emmett–Teller (BET) analysis via nitrogen adsorption and desorption measurement (Fig. 6). The BET surface area of active carbon is 1255.3 m<sup>2</sup> g<sup>-1</sup>. The inset in Fig. 6 displays the distribution of the pores in active carbon. Most of the pores range from 1 to 6 nm with a main peak centered at ~1.3 nm, demonstrating the microporous feature. Such porous structure with large specific surface area can provide lots of sites for Fe<sub>3</sub>O<sub>4</sub> deposition during solvothermal process. The nano-pores cannot only effectively hold the Fe<sub>3</sub>O<sub>4</sub> particles to form mosaic structure, but also accommodate the volume change of Fe<sub>3</sub>O<sub>4</sub> during lithiation/delithiation process, prevent



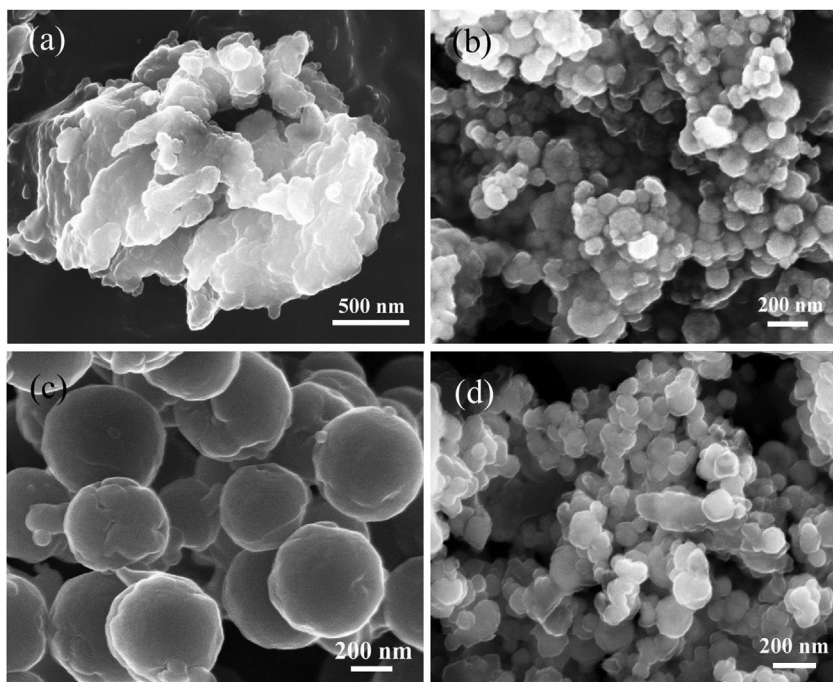


Fig. 4. FE-SEM images of active carbon before (a) and after (b) solvothermal treatment, and the synthesized bare Fe<sub>3</sub>O<sub>4</sub> (c) and Fe<sub>3</sub>O<sub>4</sub>@C nanocomposite (d).

the cracking and/or divorcing of active particle and thereby keep the integrity of electrode.

Fig. 5b and c also show that the synthesized Fe<sub>3</sub>O<sub>4</sub>@C sample displays spherical particle morphology with average diameter of ca. 100 nm. Even in Fe<sub>3</sub>O<sub>4</sub>@C particle, lots of micropores are visible, implying that not all of the pores of active carbon are filled by the deposited Fe<sub>3</sub>O<sub>4</sub>. The possible situation is that most of the Fe<sub>3</sub>O<sub>4</sub> deposited from solution on the surface pores of active carbon particles. HR-TEM observation on the surface of Fe<sub>3</sub>O<sub>4</sub>@C particle was performed and the image is shown in Fig. 5d. The clear and

continuous lattice fringes indicate the high crystallinity of the material. Two different interplanar spacings of 0.290 and 0.492 nm are identified, which agree well to (220) and (111) planes of Fe<sub>3</sub>O<sub>4</sub>. Combined with the electron diffraction pattern shown in the inset of Fig. 5d, it is reasonable to state that the surface component of Fe<sub>3</sub>O<sub>4</sub>@C particle is highly crystallized Fe<sub>3</sub>O<sub>4</sub> nanoparticles. To confirm that the Fe<sub>3</sub>O<sub>4</sub> nanocrystals are dispersed in the microporous carbon matrix, the elemental mapping of C, O, and Fe was performed. The STEM image is displayed in Fig. 7a, while the elemental mapping results for region A in Fig. 7a are presented in Fig. 7b, c and d, respectively, for the elemental mapping of C, O and Fe. As it can be seen, the dark spots of Fig. 7b (carbon), corresponding to the pores of active carbon, make a shape similar to the bright spots of Fig. 7c (oxygen) and d (ferrum), demonstrating that the Fe<sub>3</sub>O<sub>4</sub> particles are filled in the pores of active carbon particles.

According to the XRD, FE-SEM, TEM and STEM/EDX results, an illustration of the possible formation process of Fe<sub>3</sub>O<sub>4</sub>@C is presented in Fig. 8. The active carbon with blob-like morphology, high

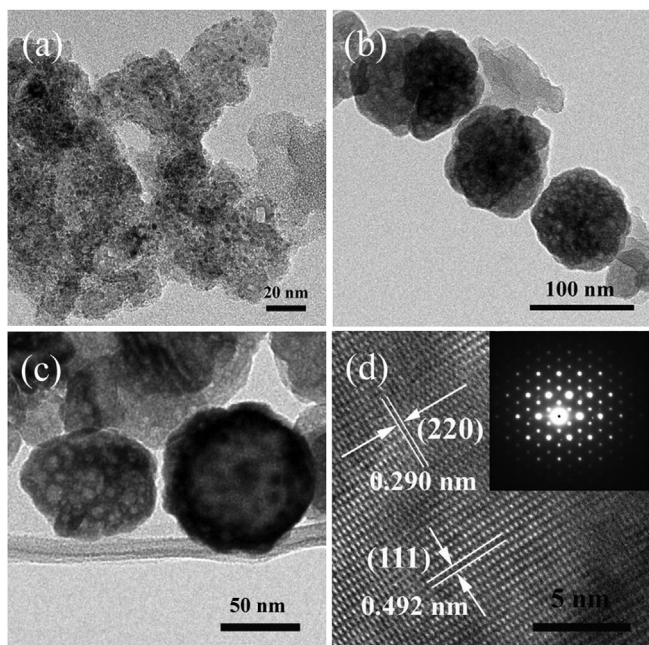


Fig. 5. TEM images of active carbon (a) and Fe<sub>3</sub>O<sub>4</sub>@C (b, c) and HR-TEM micrographs (inset: selected area diffraction image) of the Fe<sub>3</sub>O<sub>4</sub>@C (d).

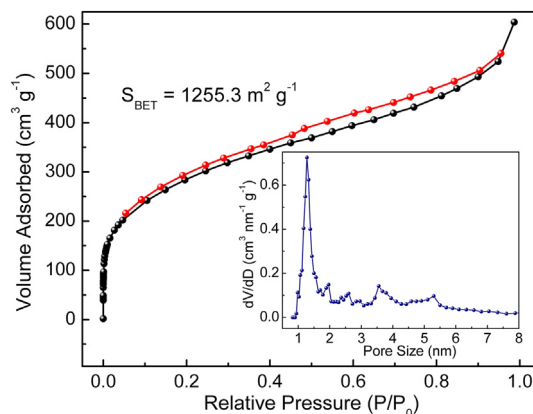
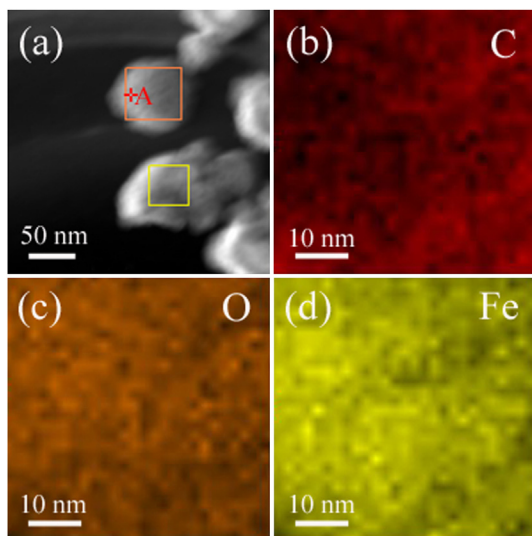


Fig. 6. N<sub>2</sub> adsorption/desorption isotherms of active carbon after solvothermal treatment. (inset: BJH pore size distribution of the corresponding sample.)



**Fig. 7.** (a) STEM image of Fe<sub>3</sub>O<sub>4</sub>@C nanoparticles and EDX mapping of C (b), O (c) and Fe (d) elements for the indicated area in (a).

porosity and high specific surface area was employed as host. Under solvothermal condition in FeCl<sub>3</sub> solution, the active carbon was spheroidized firstly, and then the Fe<sub>3</sub>O<sub>4</sub> particles were precipitate from the solution and deposited on the surface pores of the active carbon, forming a mosaic structured Fe<sub>3</sub>O<sub>4</sub>@C composite. The formation of Fe<sub>3</sub>O<sub>4</sub> on active carbon was a heterogeneous nucleation process [40], i.e. the active carbon acted as nucleus and the Fe<sub>3</sub>O<sub>4</sub> crystallized and grown inside the surface pores as well as the outer surface of active carbon particles, producing a core (carbon)/shell (Fe<sub>3</sub>O<sub>4</sub>) structure with mosaic characteristics. The porous characteristic of active carbon ensured the uniform deposition and the tight combination of Fe<sub>3</sub>O<sub>4</sub> on the surface of active carbon.

The electrochemical properties of the as-prepared bare Fe<sub>3</sub>O<sub>4</sub> and Fe<sub>3</sub>O<sub>4</sub>@C samples were evaluated by charge/discharge measurements at a current density of 100 mA g<sup>-1</sup> over a potential window of 0.02–3.0 V. The charge/discharge curves of the initial 30 cycles of the Fe<sub>3</sub>O<sub>4</sub> and Fe<sub>3</sub>O<sub>4</sub>@C are shown in Fig. 9. The steep voltage drop from about 2.3 to 0.8 V is attributed to Li ion insertion into the Fe<sub>3</sub>O<sub>4</sub> lattice ( $\text{Fe}_3\text{O}_4 + x\text{Li}^+ + xe^- \rightarrow \text{Li}_x\text{Fe}_3\text{O}_4$ ), while the long obvious potential plateau at about 0.8 V corresponds to the reversible reduction from Fe<sup>3+</sup> (or Fe<sup>2+</sup>) to Fe<sup>0</sup> ( $\text{Li}_x\text{Fe}_3\text{O}_4 + (8-x)\text{Li}^+ + (8-x)e^- \rightarrow 4\text{Li}_2\text{O} + 3\text{Fe}$ ) and the irreversible formation of solid electrolyte interphase (SEI) film [21,30,32–34,41]. From the second cycle, this plateau increases to a little bit higher voltage and becomes much shorter, indicating the different lithiation reactions between the first and the following cycles and the existence of irreversible reactions. In the case of the Fe<sub>3</sub>O<sub>4</sub>@C composite, the first discharge curve is very similar to that of bare Fe<sub>3</sub>O<sub>4</sub>, except for

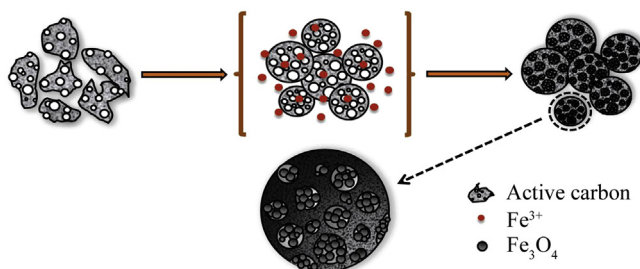


**Fig. 8.** Possible formation mechanism of nanostructured Fe<sub>3</sub>O<sub>4</sub>@C.

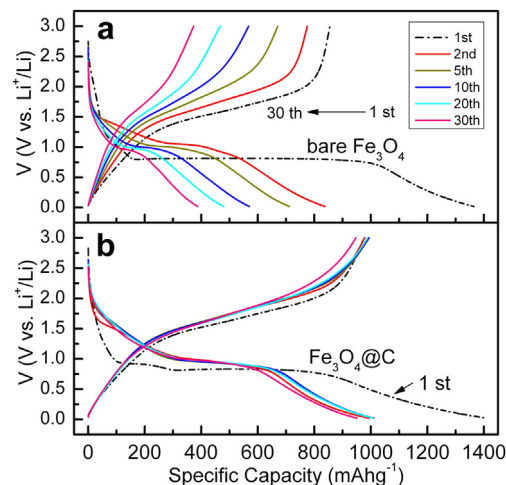


**Fig. 9.** Discharge/charge profiles of the bare Fe<sub>3</sub>O<sub>4</sub> (a) and Fe<sub>3</sub>O<sub>4</sub>@C (b) electrodes.

a potential plateau at ~0.9 V. This plateau should be related to the active carbon, which is frequently found in the reported works about iron oxide/carbon anodes [41,42]. With cycling, the specific capacity of the bare Fe<sub>3</sub>O<sub>4</sub> fades quickly, while the Fe<sub>3</sub>O<sub>4</sub>@C presents a much stabler specific capacity with the discharge/charge curves overlapped together, indicating a highly reversible electrode reaction process and a stable electrode structure characteristic.

The cyclic performance of the Fe<sub>3</sub>O<sub>4</sub>@C composite is illustrated in Fig. 10a at a current density of 100 mA g<sup>-1</sup> for 40 cycles. The bare Fe<sub>3</sub>O<sub>4</sub> sample was also investigated for comparison at the same condition. The prepared Fe<sub>3</sub>O<sub>4</sub>@C composite exhibits a high specific capacity (ca. 1000 mAh g<sup>-1</sup>) and good cycling stability, while the bare Fe<sub>3</sub>O<sub>4</sub> sample displays a slightly lower specific capacity and fast performance decline, only 333.9 mAh g<sup>-1</sup> is remained after 40 cycles. Except for the first cycle, the Fe<sub>3</sub>O<sub>4</sub>@C composite exhibits the coulombic efficiency close to 100%, indicating an excellent reversibility of electrode reaction.

Taking into account of the electrochemical reversible reaction of Fe<sub>3</sub>O<sub>4</sub> and the TG result, the theoretical capacity (C) of the synthesized Fe<sub>3</sub>O<sub>4</sub>@C can be calculated [43–46].

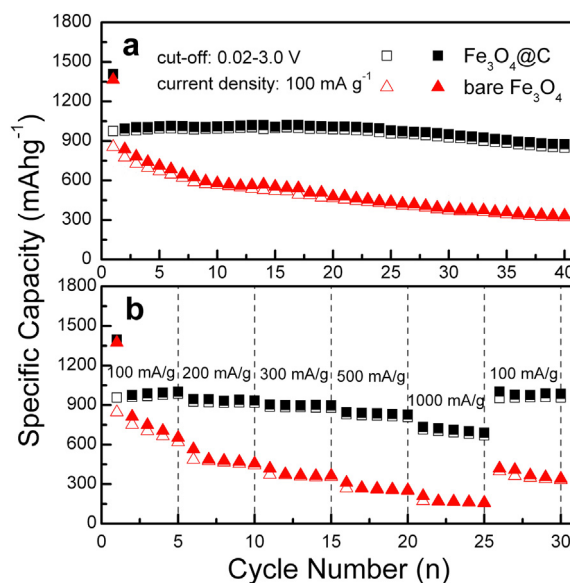


**Fig. 10.** Cycling performances (a) and rate capability (b) of bare Fe<sub>3</sub>O<sub>4</sub> and Fe<sub>3</sub>O<sub>4</sub>@C composite electrodes.



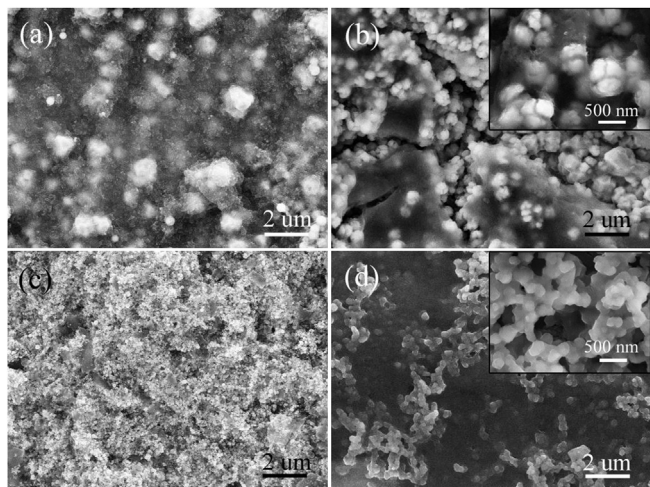


Fig. 11. SEM images of  $\text{Fe}_3\text{O}_4$  (a, b) and  $\text{Fe}_3\text{O}_4@\text{C}$  (c, d) electrodes before (a, c) and after (b, d) 10 cycles.

$$\begin{aligned} C(\text{theoretical}) &= C(\text{Fe}_3\text{O}_4) \times \text{mass percentage of Fe}_3\text{O}_4 \\ &\quad + C(\text{graphite}) \times \text{mass percentage of graphite} \\ &= 926 \times 78\% + 372 \times 18\% = 789 \text{ mAh g}^{-1} \end{aligned}$$

The reversible capacity of the  $\text{Fe}_3\text{O}_4@\text{C}$  composite, as shown in Fig. 10a, is much higher than the theoretical capacity of the  $\text{Fe}_3\text{O}_4$  ( $926 \text{ mAh g}^{-1}$ ) and the theoretical prediction value for  $\text{Fe}_3\text{O}_4@\text{C}$ . The extra capacity is probably due to the reversible trapping of  $\text{Li}^+$  in the micropores of the  $\text{Fe}_3\text{O}_4@\text{C}$  at lower voltage, as proposed by Sonobe et al. [47] and Tokumitsu et al. [48]. In addition, the reversible growth of a polymeric gel-like film resulting from kinetically activated electrolyte degradation also makes a contribution to the extra capacity [49,50].

The rate capability of the prepared bare  $\text{Fe}_3\text{O}_4$  and  $\text{Fe}_3\text{O}_4@\text{C}$  composite was evaluated by cycling the electrode in a step mode at different current densities. The results are shown in Fig. 10b. The  $\text{Fe}_3\text{O}_4@\text{C}$  composite exhibits higher specific capacity and stable cycling performance at each current density. A specific capacity of  $702 \text{ mAh g}^{-1}$  can still be delivered by  $\text{Fe}_3\text{O}_4@\text{C}$  composite at  $1000 \text{ mA g}^{-1}$ , 70% of the capacity at  $100 \text{ mA g}^{-1}$ . When the current density switches back from  $1000 \text{ mA g}^{-1}$  to  $100 \text{ mA g}^{-1}$ , the specific capacity can be recovered perfectly, demonstrating the excellent rate capability and good structural stability of the  $\text{Fe}_3\text{O}_4@\text{C}$  electrode. However, the bare  $\text{Fe}_3\text{O}_4$  shows dramatic capacity degradation with increasing charge/discharge current density, only  $132 \text{ mAh g}^{-1}$  is remained when cycled at  $1000 \text{ mA g}^{-1}$ . The declined specific capacity of the bare  $\text{Fe}_3\text{O}_4$  cannot be rehabilitated even when the current density is switched back  $100 \text{ mA g}^{-1}$ , implying the destruction of the electrode.

The much better electrochemical performance of the  $\text{Fe}_3\text{O}_4@\text{C}$  composite in terms of specific capacity, cycling stability and rate capability can be ascribed to the unique core/shell and mosaic structure and the carbon conductive network. The nanosized feature of  $\text{Fe}_3\text{O}_4$  on the active carbon surface ensures the complete lithiation reaction and thereby the high specific capacity of electrode [24,51–54], while the active carbon provided large amount of surface pores to anchor the  $\text{Fe}_3\text{O}_4$  nanoparticles effectively, thus to keep the integrity of the electrode. Furthermore, the good adherence between  $\text{Fe}_3\text{O}_4$  and carbon matrix enhances the electron and lithium ion conduction, which significantly facilitates the electrode reaction kinetic process and therefore improves the rate performance compared with the bare  $\text{Fe}_3\text{O}_4$  [18,19,24,52]. The existence

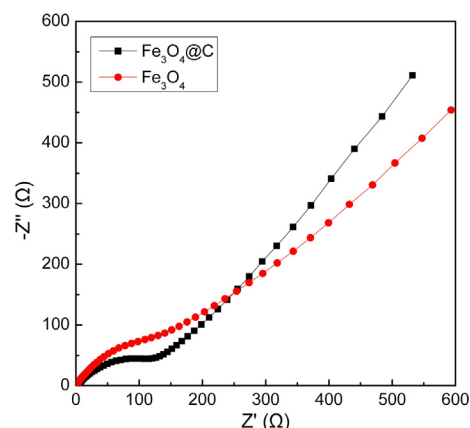


Fig. 12. Nyquist plots of  $\text{Fe}_3\text{O}_4@\text{C}$  and  $\text{Fe}_3\text{O}_4$  electrodes after 3 cycles.

of the active carbon can also prevent the  $\text{Fe}_3\text{O}_4$  particles from aggregation, and the pores in active carbon can effectively buffer the volume change of  $\text{Fe}_3\text{O}_4$  caused by lithiation/delithiation, and thereby leading to an excellent cycling stability.

To further understand the effects of the carbon matrix on the electrode integrity, the electrode surface of  $\text{Fe}_3\text{O}_4$  and  $\text{Fe}_3\text{O}_4@\text{C}$  before and after 10 cycles was observed by SEM. The results are illustrated in Fig. 11. The active material, electrical conductor and binder are homogeneously distributed in both of the two electrodes before cycling, as shown in Fig. 11a and c. After 10 cycles, however, the  $\text{Fe}_3\text{O}_4$  electrode cracks severely (Fig. 11b), and even the  $\text{Fe}_3\text{O}_4$  particles are pulverized, as shown in the inset. On the contrary, the  $\text{Fe}_3\text{O}_4@\text{C}$  electrode maintains good geometric integrity without any particle cracking after 10 cycles (Fig. 11d). This difference between the two electrodes is apparently caused by the different particle structures of  $\text{Fe}_3\text{O}_4$  with  $\text{Fe}_3\text{O}_4@\text{C}$ . The active carbon with high specific surface area tends to attract and grasp firmly the crystallized  $\text{Fe}_3\text{O}_4$  so as to decrease the huge specific surface energy. The formed special core/shell structure of  $\text{Fe}_3\text{O}_4@\text{C}$  particle has a strong structural stability and is tough against the volume and stress variation of  $\text{Fe}_3\text{O}_4$  component during cycling, leading to a good integrity of electrode and thereby an excellent cycling stability of  $\text{Fe}_3\text{O}_4$ -based electrode.

AC impedance measurements are further conducted to elucidate the electrode reaction features. Fig. 12 shows the Nyquist plots of the two electrodes after 3 cycles (at  $100 \text{ mA g}^{-1}$ ) in the fully charged state. Both profiles consist of a semicircle in the high-frequency region associated with the SEI film and charge transfer resistances, and a long low-frequency line corresponding to the lithium-diffusion process within electrodes. Considering that the SEI polymeric gel film is decomposed at fully charge state for iron oxide-based electrode [55], it is reasonable to attribute the high frequency arc mainly to the charge transfer process. Obviously, the intercept of the semicircle with real axis for the  $\text{Fe}_3\text{O}_4@\text{C}$  electrode is much smaller than that of the  $\text{Fe}_3\text{O}_4$  electrode, indicating that the  $\text{Fe}_3\text{O}_4@\text{C}$  electrode displays smaller charge transfer resistance. This means that the electrode reaction can process more effectively in  $\text{Fe}_3\text{O}_4@\text{C}$  electrode due to the existence of active carbon matrix and nano-sized  $\text{Fe}_3\text{O}_4$ . The enhanced electrode reaction kinetics leads to a better electrochemical performance of the  $\text{Fe}_3\text{O}_4@\text{C}$  electrode.

#### 4. Conclusion

We demonstrate a facial solvothermal route for the construction and synthesis of highly dispersed  $\text{Fe}_3\text{O}_4@\text{C}$  spheres with an average size of ca. 100 nm. The porous active carbon provides an effective

matrix for the dispersion of  $\text{Fe}_3\text{O}_4$  particles. The formation of  $\text{Fe}_3\text{O}_4$  is a heterogeneous nucleation process. The active carbon acts as nuclei and the  $\text{Fe}_3\text{O}_4$  precipitates and grows on the surface pores of active carbon, forming a core (carbon)/shell ( $\text{Fe}_3\text{O}_4$ ) structure with mosaic characteristics. The unique porous carbon provides space to accommodate the volume variation of active  $\text{Fe}_3\text{O}_4$  and helps to keep the integrity of  $\text{Fe}_3\text{O}_4/\text{C}$  active particle and therefore corresponding electrode. The good contact between  $\text{Fe}_3\text{O}_4$  and carbon matrix ensures the fast electron/Li-ion transport. As a result, the  $\text{Fe}_3\text{O}_4/\text{C}$  composite exhibits high reversible capacity, good cycling stability and excellent rate capability. For practical applications, we believe that the prepared  $\text{Fe}_3\text{O}_4/\text{C}$  composite is a potential candidate for anode material of high-performance lithium-ion battery.

## Acknowledgments

This work was financially supported by National Basic Research Program of China (2013CB934003), National Nature Science Foundation of China (21273019) and the Fundamental Research Funds for the Central Universities (FRF-MP-12-006B).

## References

- [1] P.G. Bruce, B. Scrosati, J.-M. Tarascon, *Angew. Chem. Int. Ed.* 47 (2008) 2930–2946.
- [2] Y.-G. Guo, J.-S. Hu, L.-J. Wan, *Adv. Mater.* 20 (2008) 2878–2887.
- [3] H. Li, Z. Wang, L. Chen, X. Huang, *Adv. Mater.* 21 (2009) 4593–4607.
- [4] M.G. Kim, J. Cho, *Adv. Funct. Mater.* 19 (2009) 1497–1514.
- [5] G. Jeong, Y.-U. Kim, H. Kim, Y.-J. Kim, H.-J. Sohn, *Energy Environ. Sci.* 4 (2011) 1986–2002.
- [6] H. Li, H. Zhou, *Chem. Commun.* 48 (2012) 1201–1217.
- [7] Y. Liu, D. Liu, Q. Zhang, G. Cao, *J. Mater. Chem.* 21 (2011) 9969–9983.
- [8] H.-S. Lim, B.-Y. Jung, Y.-K. Sun, K.-D. Suh, *Electrochim. Acta* 75 (2012) 123–130.
- [9] A.S. Aricò, P. Bruce, B. Scrosati, J.-M. Tarascon, W.V. Schalkwijk, *Nat. Mater.* 4 (2005) 366–377.
- [10] P. Poizot, S. Laruelle, S. Grugeon, L. Dupont, J.-M. Tarascon, *Nature* 407 (2000) 496–499.
- [11] T. Muraliganth, A.V. Murugan, A. Manthiram, *Chem. Commun.* 47 (2009) 7360–7362.
- [12] W.-M. Zhang, X.-L. Wu, J.-S. Hu, Y.-G. Guo, L.-J. Wan, *Adv. Funct. Mater.* 18 (2008) 3941–3946.
- [13] A. Ito, L. Zhao, S. Okada, J. Yamaki, *J. Power Sources* 196 (2011) 8154–8159.
- [14] G. Zhou, D.-W. Wang, F. Li, L. Zhang, N. Li, Z.-S. Wu, L. Wen, G.Q. Lu, H.-M. Cheng, *Chem. Mater.* 22 (2010) 5306–5313.
- [15] J. Jiang, Y. Li, J. Liu, X. Huang, *Nanoscale* 3 (2011) 45–48.
- [16] B. Banov, L. Ljutzkanov, I. Dimitrov, A. Trifonova, H.J. Vasilchina, *Nano Sci. Nano Technol.* 8 (2008) 591–594.
- [17] W.X. Chen, J.Y. Lee, Z. Liu, *Electrochem. Commun.* 4 (2002) 260–265.
- [18] Z. Wang, L. Zhou, X.W. Lou, *Adv. Mater.* 24 (2012) 1903–1911.
- [19] Y. Zhai, Y. Dou, D. Zhao, R.F. Fulvio, R.T. Mayes, S. Dai, *Adv. Mater.* 23 (2011) 4828–4850.
- [20] Y. Chen, H. Xia, L. Lu, J. Xue, *J. Mater. Chem.* 22 (2012) 5006–5012.
- [21] P. Wu, N. Du, H. Zhang, J. Yu, D. Yang, *J. Phys. Chem. C* 115 (2011) 3612–3620.
- [22] M. Zhang, X. Yin, Z. Du, S. Liu, L. Chen, Q. Li, H. Jin, K. Peng, T. Wang, *Solid State Sci.* 12 (2010) 2024–2029.
- [23] T. Zhu, J.S. Chen, X.W. Lou, *J. Phys. Chem. C* 115 (2011) 9814–9820.
- [24] Q.Q. Xiong, Y. Lu, X.L. Wang, C.D. Gu, Y.Q. Qiao, J.P. Tu, *J. Alloys Compd.* 536 (2012) 219–225.
- [25] S.M. Yuan, J.X. Li, L.T. Yang, L.W. Su, L. Liu, Z. Zhou, *ACS Appl. Mater. Interfaces* 3 (2011) 705–709.
- [26] E. Kang, Y.S. Jung, A.S. Cavanagh, G. Kim, S.M. George, A.C. Dillon, J.K. Kim, J. Lee, *Adv. Funct. Mater.* 21 (2011) 2430–2438.
- [27] L. Marcos, A. Primo, H. Garcia, *J. Mater. Chem.* 22 (2012) 21373–21375.
- [28] T. Yoon, C. Chae, Y.-K. Sun, X. Zhao, H. Kung, J.K. Lee, *J. Mater. Chem.* 21 (2011) 17325–17330.
- [29] M. Sathish, T. Tomai, I. Honma, *J. Power Sources* 217 (2012) 85–91.
- [30] J. Su, M. Cao, L. Ren, C. Hu, *J. Phys. Chem. C* 115 (2011) 14469–14477.
- [31] Q. Wang, L. Jiao, H. Du, Y. Wang, H. Yuan, *J. Power Sources* 245 (2014) 101–106.
- [32] E. Frackowiak, F. Béguin, *Carbon* 39 (2001) 937–950.
- [33] A. Kucinska, A. Cyganiuk, J.P. Lukaszewicz, *Carbon* 50 (2012) 3092–3116.
- [34] X. Zhao, D. Xia, K. Zheng, *ACS Appl. Mater. Interfaces* 4 (2012) 1350–1356.
- [35] Q. Hao, D. Lei, X. Yin, M. Zhang, S. Liu, Q. Li, L. Chen, T. Wang, *J. Solid State Electrochem.* 15 (2011) 2563–2569.
- [36] J. Zheng, Z. Liu, X. Zhao, M. Liu, X. Liu, W. Chu, *Nanotechnology* 23 (2012) 165601–165608.
- [37] Y. Hu, Y. Shan, K. Chen, *Mater. Res. Bull.* 43 (2008) 2703–2708.
- [38] K. Zhou, Y. Zhu, X. Yang, C. Li, New J. Chem. 34 (2010) 2950–2955.
- [39] S. Xuan, L. Hao, W. Jiang, X. Gong, Y. Hu, Z. Chen, *Nanotechnology* 18 (2007) 035602–035607.
- [40] W.D. Kingery, H.K. Bowen, D.R. Uhlmann, *Introduction to Ceramics*, John Wiley & Sons Inc, Canada, 1976, p. 328.
- [41] S. Jin, H. Deng, D. Long, X. Liu, L. Zhan, X. Liang, W. Qiao, L. Ling, *J. Power Sources* 196 (2011) 3887–3893.
- [42] Y. Deng, Q. Zhang, Z. Shi, L. Han, F. Peng, G. Chen, *Electrochim. Acta* 76 (2012) 495–503.
- [43] P. Poizot, S. Laruelle, S. Grugeon, J.-M. Tarascon, *Electrochem. Soc.* 149 (2002) A1212–A1217.
- [44] D. Li, M.B. Müller, S. Gilje, R.B. Kaner, G.G. Wallace, *Nat. Nanotechnol.* 3 (2008) 101–105.
- [45] B. Li, H. Cao, J. Shao, G. Li, M. Qu, G. Yin, *Inorg. Chem.* 50 (2011) 1628–1632.
- [46] B. Li, H. Cao, J. Shao, M. Qu, J.H. Warner, *J. Mater. Chem.* 21 (2011) 5069–5075.
- [47] N. Sonobe, M. Ishikawa, T. Iwasaki, in: *Extended Abstracts of the 35th Battery Symposium Nov. 14–16, Paper 2B10*, Nagoya, Japan, vol. 49, 1994.
- [48] K. Tokumitsu, H. Fujimoto, A. Mabuchi, T. Kasuh, *Carbon* 37 (1999) 1599–1605.
- [49] S. Grugeon, S. Laruelle, L. Dupont, J.-M. Tarascon, *Solid State Sci.* 5 (2003) 895–904.
- [50] J. Do, C. Weng, *J. Power Sources* 146 (2005) 482–486.
- [51] S.K. Behera, *J. Power Sources* 196 (2011) 8669–8674.
- [52] S. Wang, J. Zhang, C. Chen, *J. Power Sources* 195 (2010) 5379–5381.
- [53] H.-S. Kim, S.H. Baek, M.-W. Jang, Y.-K. Sun, C.S. Yoon, *J. Electrochem. Soc.* 159 (2012) A325–A329.
- [54] K.T. Lee, J. Cho, *Nano Today* 6 (2011) 28–41.
- [55] S. Laruelle, S. Grugeon, P. Poizot, M. Dollé, L. Dupont, J.-M. Tarascon, *J. Electrochem. Soc.* 149 (2002) A627–A634.